Supporting Information for

"The role of current sheet scattering in the proton isotropic boundary formation during geomagnetic storms"

John D. Haiducek[1], Natalia Y. Ganushkina[2,3], Stepan Dubyagin[3], Daniel T. Welling[2,4]

[1]U.S. Naval Research Laboratory, Washington, DC, USA

[2]Climate and Space Sciences, University of Michigan, Ann Arbor, MI, USA

[3]Finnish Meteorological Institute, Helsinki, Finland

[4]University of Texas at Arlington, Arlington, TX, USA

Contents

Additional Supporting Information (Files uploaded separately)

1. Caption for Data Set S1
2. Caption for Data Set S2
3. Caption for Data Set S3

Additional correction based on $\frac{dBz}{dr}$

This section describes an additional correction procedure which was introduced in Haiducek, Ganushkina, Dubyagin, and Welling (2019 *accepted*). It proved ineffective for the data presented in this paper, and was therefore not applied to the final results of the paper. The basis of the procedure is that, in addition to the dependence on B_z, Equation 2 shows that K should depend on $G = \frac{dB_r}{dz}$. Using the THEMIS magnetic field measurements we can estimate the gradient of B_r in the z direction, which depends on current sheet strength and thickness. Larger values of this gradient indicate either a thin-

Corresponding author: John D. Haiducek, jhaiduce@umich.edu

ner current sheet or stronger current. Using THEMIS spacecraft that are conjugate with an IB observation as, we estimate $G = \frac{dBr}{dz}$

$$G = \frac{B_{r_1} - B_{r_2}}{z_1 - z_2}, \tag{1}$$

where the subscripts 1 and 2 denote members of a pair of THEMIS spacecraft.

Figure S8 shows a time-series of observed magnetic fields at THEMIS A, D, and E, with B_r shown in Figure S8a and B_z shown in Figure S8b. The spacecraft are identified by color in the same manner as Figure 2. B_r was often quite different at THEMIS A than at THEMIS D or E, while values of B_z remained very close between all three spacecraft. On the other hand, it is not clear that the difference in B_r is always sufficient for accurate estimation of gradients in z. We therefore developed a procedure to determine whether the spacecraft are suitably positioned for accurate estimation of G. To this end, we define

$$\phi = \tan^{-1}\left(\frac{\sqrt{(x_1 - x_2)^2 + (y_1 - y_2)^2}}{|z_1 - z_2|}\right) \tag{2}$$

as an angle parameterizing the z-alignment of the two spacecraft, where x, y, and z are components of the spacecraft location in GSM coordinates. In addition, we define

$$\theta = \tan^{-1}\left(\frac{\sqrt{B_x^2 + B_y^2}}{B_z}\right), \tag{3}$$

which roughly corresponds to the distance from the neutral sheet.

To select pairs of spacecraft for G estimation we apply the following rules to the THEMIS spacecraft that are conjugate with each observed IB location:

1. If more than two spacecraft are conjugate with the IB, the pair with the smallest ϕ is selected. This minimizes the spacecraft's displacement relative to each other in the x-y plane, relative to their z displacement.
2. Pairs for which $\phi > 45°$ are rejected. This ensures that the displacement between the spacecraft in the x-y plane is not too large compared with the z displacement.
3. Pairs for which $\theta > 45°$ at either satellite are rejected, in order to use only pairs located near the neutral sheet.

4. Pairs for which $\Delta z = |z_1 - z_2| < 0.2$ are rejected, to ensure that displacement in z is large enough for accurate gradient estimation.

Overall, we found that SWMF has a slight tendency to overestimate $|G|$, though significant differences are apparent among the individual simulations. Statistics for the distribution of $|G|$ are given in Table S3.

The $G = \frac{dB_x}{dz}$ estimates obtained using the THEMIS spacecraft enable an additional correction of K, following the procedure introduced in Haiducek et al. (2019 *accepted*). Figure S9 shows K^* as a function of $\Delta|G| = |G|_{model} - |G|_{obs}$, with the HL data in Figure S9a and the LL data in Figure S9b. Both G_{model} and G_{obs} are obtained using Equation 1. MHD simulations are plotted using triangles, and empirical models using squares, with their colors identifying individual simulations or models following the color schemes from Figures 5 and 6. Log-linear fits through all the data points are drawn in black.

Figure S9 shows a weak negative correlation between K^* and $\Delta|G|$ in both the HL and LL data. While the scatter is very large, the fit shows an inverse relationship between K and $\Delta|G|$ as expected from Equation 2. We can remove the effects of this correlation simultaneously with that of $\overline{\Delta B_z}$ using a linear fit of the form

$$\log K = C_1 + C_2\overline{\Delta B_z} + C_3\Delta|G|, \tag{4}$$

where C_1, C_2, and C_3 are obtained using least squares minimization. The coefficients C_2 and C_3 serve as the basis for a new corrected value K^{**}, given by

$$K^{**} = K\exp(-C_2\overline{\Delta B_z} - C_3\Delta|G|). \tag{5}$$

We found that the distribution of K^{**} was very similar to that of K^*, and in addition the constraints placed on the positions of conjugate satellites to in an effort to obtain reliable G estimates resulted in a 90% reduction in the dataset size. These factors led to the decision not to apply it to the final results of paper. Table S4 and Figure S10 show results for K, K^*, and K^{**} using the points for which reliable G estimates could be obtained.

The estimation of G is subject to additional errors since the spacecraft used to compute the gradient in z are generally not positioned exactly in the z direction relative to

each other. The amount of separation between them in the z direction can also affect the accuracy of the gradient estimates, since separation that is too close may result in a gradient that effectively measures local structure within the current sheet rather than the overall behavior of the current sheet, while separation that is too large results in an average gradient over a long distance, which might not be representative of the gradient across the current sheet if one or both spacecraft is located too far away from the current sheet. We attempt to maximize the accuracy of our gradient estimates by selecting spacecraft pairs according to the criteria in Section 5, but the amount of accuracy provided using these criteria depends on local conditions that are not fully known. Unlike Haiducek et al. (2019 *accepted*), in which K was found to be significantly correlated with ΔG, the present paper shows very little relation between K and ΔG. This is likely due to the present work focusing on a storm-time interval, in which the current sheet is expected to be highly dynamic and the models may fail to accurately reproduce the timing, magnitude, and direction of current sheet displacement occurring in the real magnetosphere. The lack of correlation between ΔG and K is directly responsible for the similarity found between K^* and K^{**}.

Tables S1 to S4

Spacecraft	Energy (keV)
METOP-02	36.0
NOAA-15	64.8
NOAA-16	45.9
NOAA-17	45.6
NOAA-18	30.3
NOAA-19	30.0

1 Table S1: Lower energy limits for the P1 energy channels

Model	n	25th percentile (nT)	Median (nT)	75th percentile (nT)	$\overline{\Delta B_z} \leq 0$ percentage
SWMFa	199	-2.11	5.17	12.6	30.7
SWMFb	196	-3.89	5.38	14.3	31.1
SWMFc	198	-5.60	4.13	11.0	36.9
All SWMF	593	-4.57	5.15	12.7	32.9
T01	159	-11.8	-4.50	4.12	67.9
TS05	187	-4.07	1.99	7.78	42.8
TA16	181	-4.66	2.03	8.10	39.2
All empirical	527	-6.62	0.150	7.29	49.1

Table S2: Median, interquartile range, and percentage less than zero for $\overline{\Delta B_z}$.

Model	n	25th percentile (nT/R_e)	Median (nT/R_e)	75th percentile (nT/R_e)	$\Delta\lvert G\rvert \leq 0$ percentage
SWMFa	13	4.89	13.7	20.6	23.1
SWMFb	14	-6.80	-1.42	0.983	64.3
SWMFc	13	-4.24	1.05	11.5	46.2
All SWMF	40	-6.19	1.12	13.7	45.0
T01	13	-13.1	-1.26	-0.305	76.9
TS05	12	-14.1	-6.60	0.600	66.7
TA16	12	7.21	9.39	19.1	16.7
All empirical	37	-13.1	-1.18	7.21	54.1

Table S3: Median, interquartile range, and percentage less than zero for $\Delta|G|$.

Model type	IB set	n	25th percentile	Median	75th percentile	$K \leq 8$ percentage	$K \leq 13$ percentage	y axis intercept	Intercept 95% CI
				Uncorrected K					
SWMF	HL	18	8.26	13.1	16.1	22.2	50.0	—	—
SWMF	LL	22	10.1	17.0	27.7	9.09	31.8	—	—
Empirical	HL	18	7.21	10.8	14.2	38.9	61.1	—	—
Empirical	LL	19	9.27	14.3	19.1	15.8	42.1	—	—
Both	HL	36	7.40	11.8	15.1	30.6	55.6	—	—
Both	LL	41	9.23	16.4	19.8	12.2	36.6	—	—
				K^* *correction*					
SWMF	HL	18	8.13	10.1	12.3	27.8	77.8	9.84	[7.52, 12.9]
SWMF	LL	22	10.1	15.9	20.4	9.09	36.4	15.5	[11.2, 21.3]
Empirical	HL	18	7.56	10.2	13.6	44.4	66.7	9.83	[7.64, 12.6]
Empirical	LL	19	9.55	12.5	16.5	15.8	52.6	13.1	[8.75, 19.5]
Both	HL	36	7.63	10.1	13.0	30.6	75.0	9.89	[8.34, 11.7]
Both	LL	41	9.32	15.2	18.3	9.76	41.5	14.0	[11.0, 17.7]
				K^{**} *correction*					
SWMF	HL	18	8.54	10.7	12.7	16.7	77.8	10.1	[7.54, 13.6]
SWMF	LL	22	15.2	16.6	19.9	9.09	18.2	16.3	[12.3, 21.6]
Empirical	HL	18	8.04	10.5	12.6	27.8	83.3	9.46	[7.45, 12.0]
Empirical	LL	19	10.3	13.7	15.5	15.8	47.4	12.8	[8.41, 19.4]
Both	HL	36	8.72	10.4	12.7	19.4	77.8	9.98	[8.45, 11.8]
Both	LL	41	12.1	15.0	18.3	17.1	36.6	14.0	[11.2, 17.6]

Table S4: Summary of the properties of K for points for which G estimation was available.

1 Figures S1 to S8

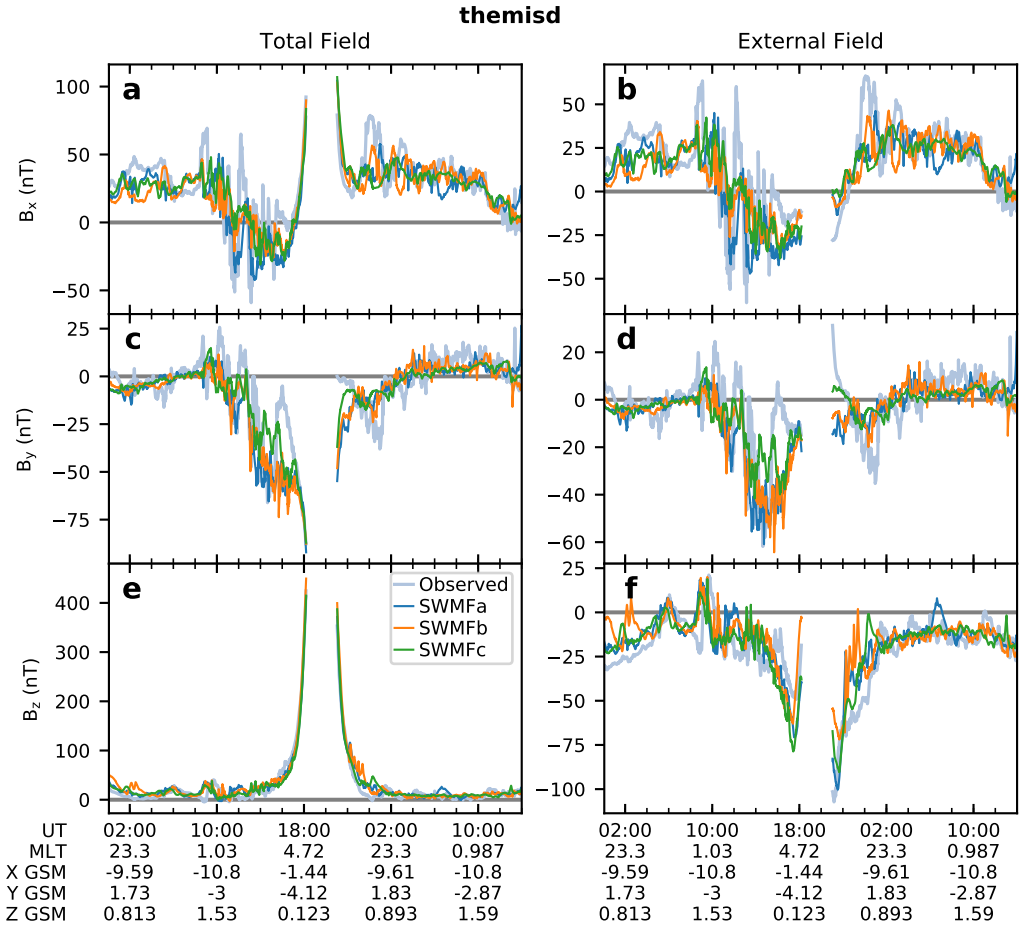

Figure S1: Magnetic field components of the total field in GSM coordinates at the THEMIS D satellite, observed and simulated, from 1200 UTC on 4 April to 1400 UTC on 6 April, 2010.

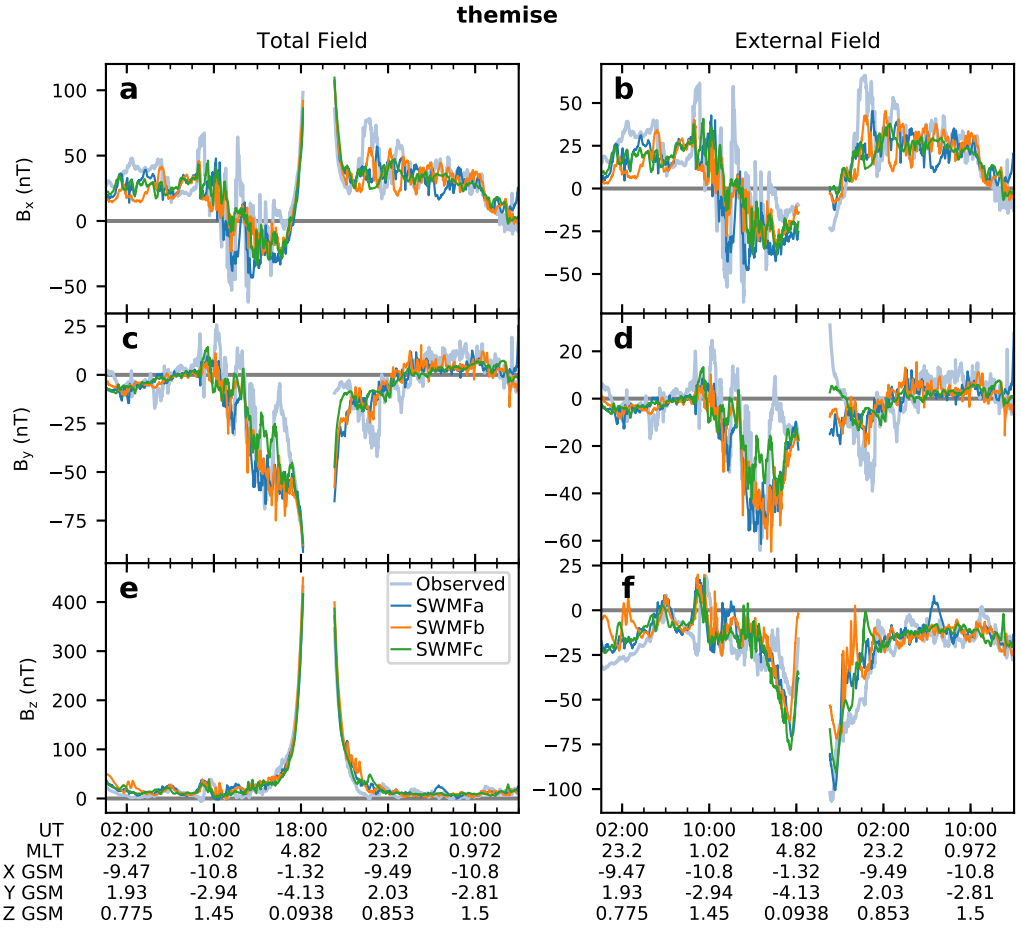

Figure S2: Magnetic field components of the total field in GSM coordinates at the THEMIS E satellite, observed and simulated, from 1200 UTC on 4 April to 1400 UTC on 6 April, 2010.

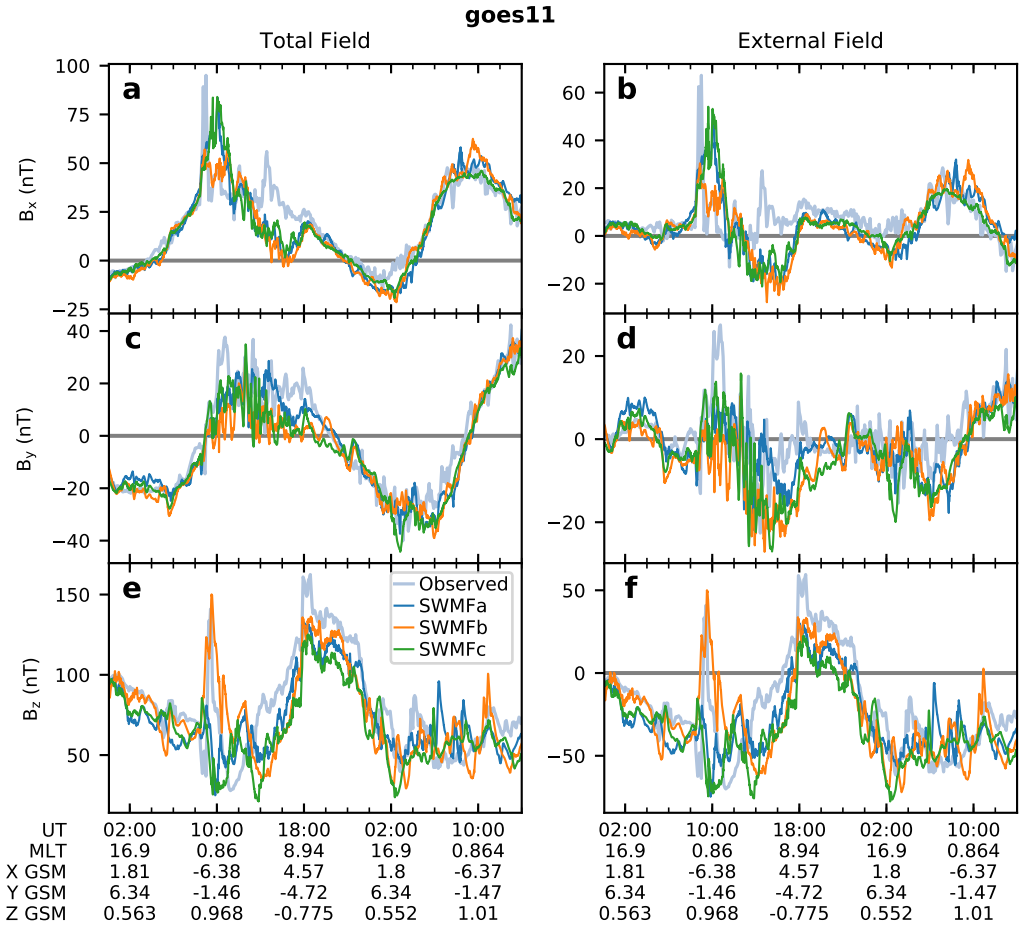

Figure S3: Magnetic field components of the total field in GSM coordinates at the GOES 11 satellite, observed and simulated, from 1200 UTC on 4 April to 1400 UTC on 6 April, 2010.

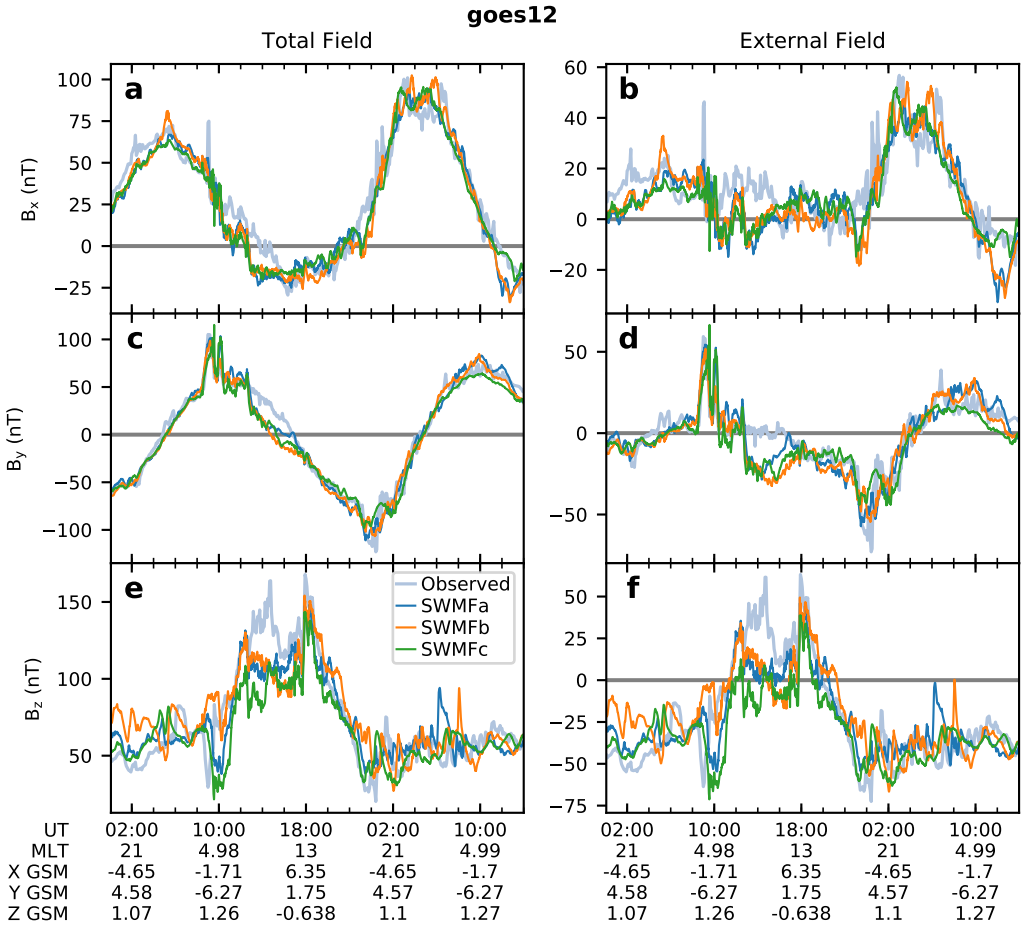

Figure S4: Magnetic field components of the total field in GSM coordinates at the GOES 12 satellite, observed and simulated, from 1200 UTC on 4 April to 1400 UTC on 6 April, 2010.

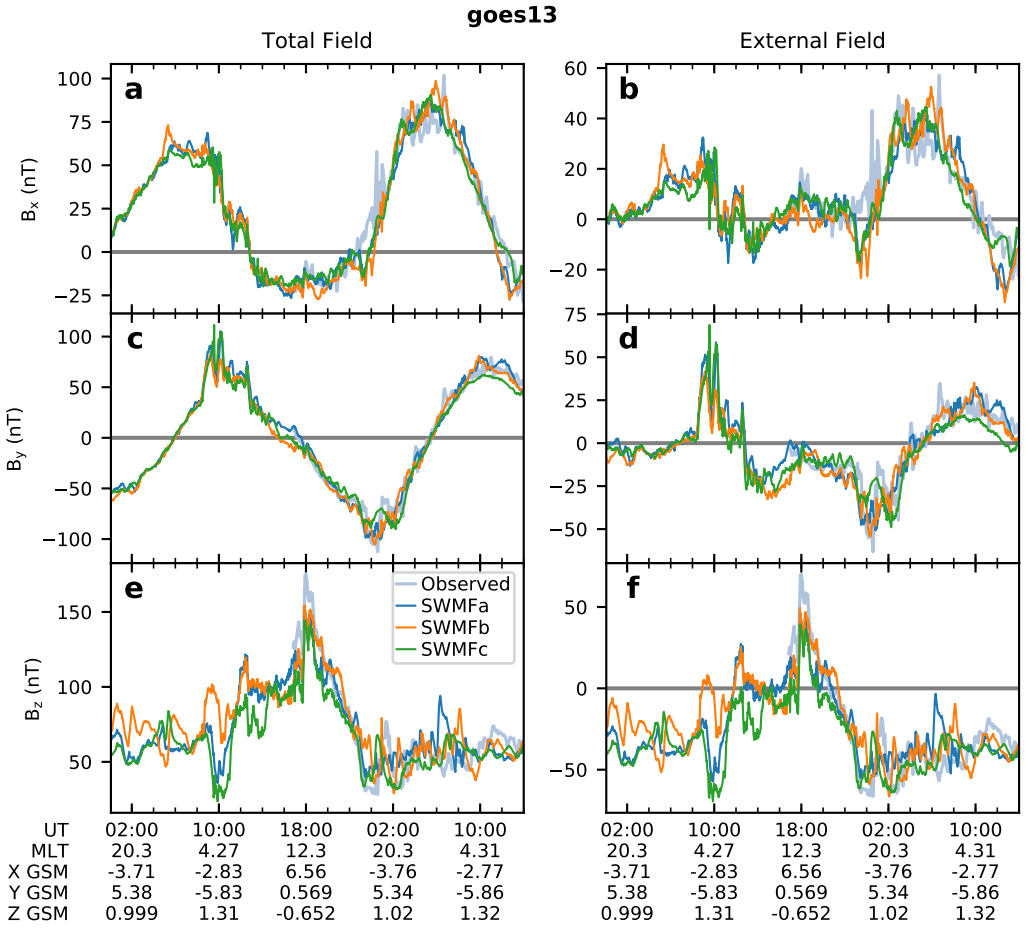

Figure S5: Magnetic field components of the total field in GSM coordinates at the GOES 13 satellite, observed and simulated, from 1200 UTC on 4 April to 1400 UTC on 6 April, 2010.

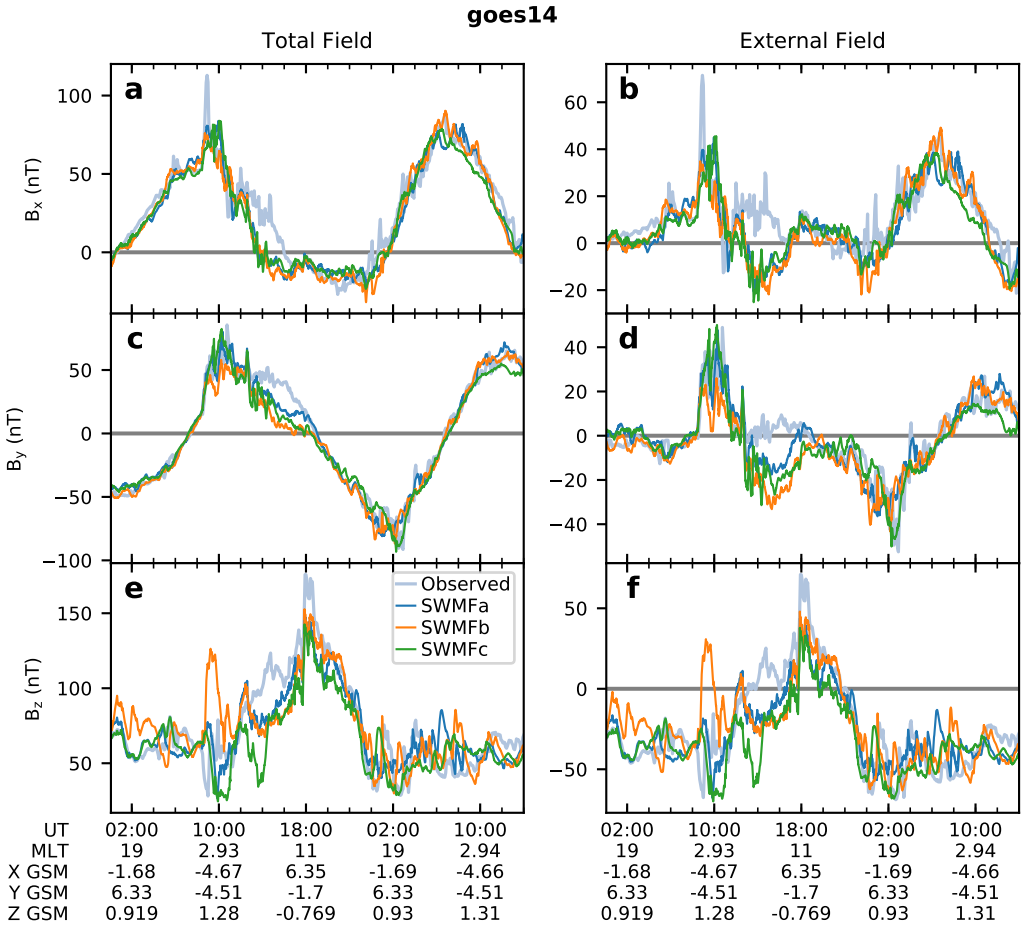

Figure S6: Magnetic field components of the total field in GSM coordinates at the GOES 14 satellite, observed and simulated, from 1200 UTC on 4 April to 1400 UTC on 6 April, 2010.

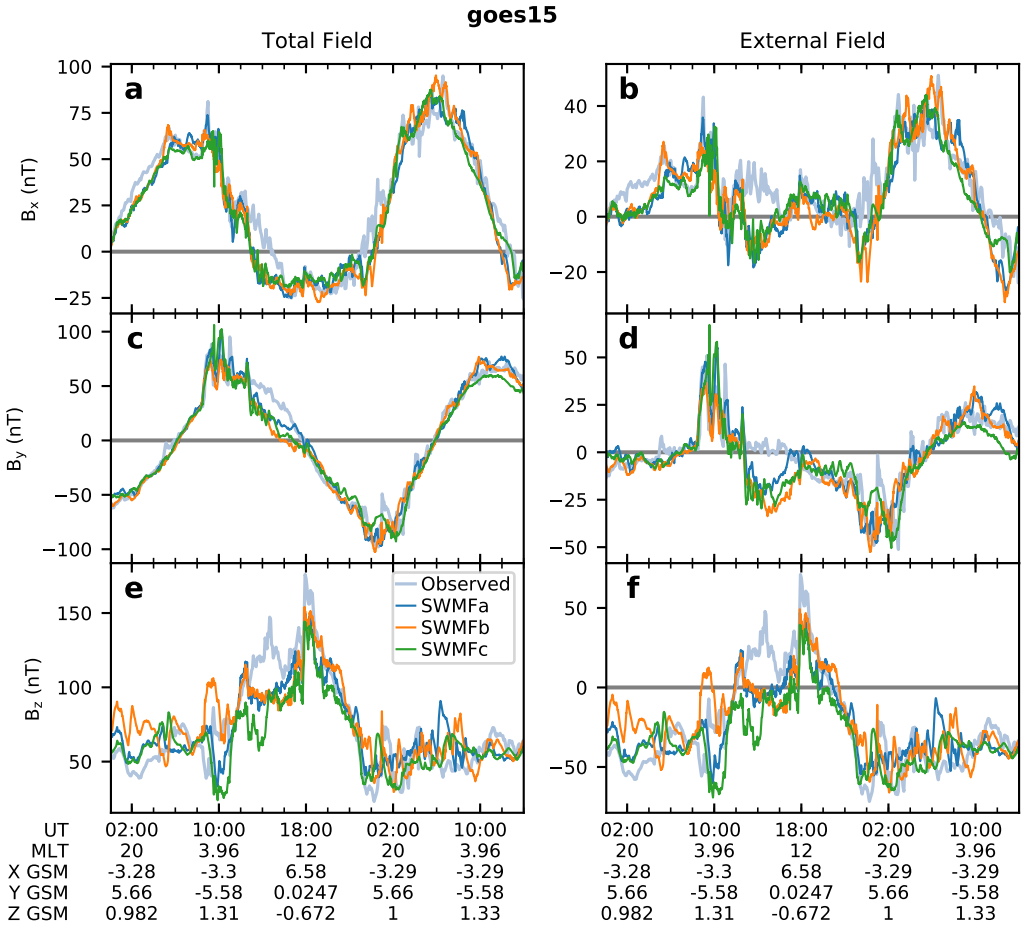

Figure S7: Magnetic field components of the total field in GSM coordinates at the GOES 15 satellite, observed and simulated, from 1200 UTC on 4 April to 1400 UTC on 6 April, 2010.

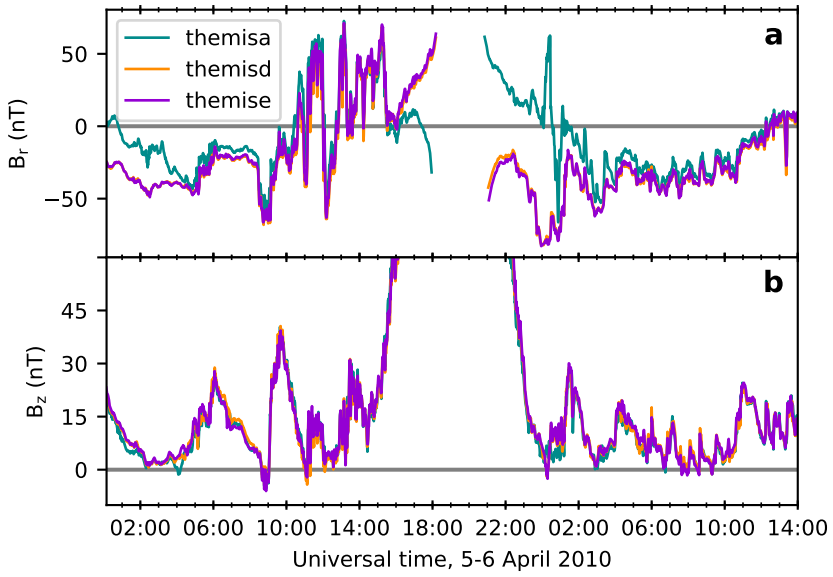

Figure S8: Observed magnetic fields at all THEMIS A, D, and E. Spacecraft are identified by color following the scheme of Figure 2. (a) B_r component (b) B_z component.

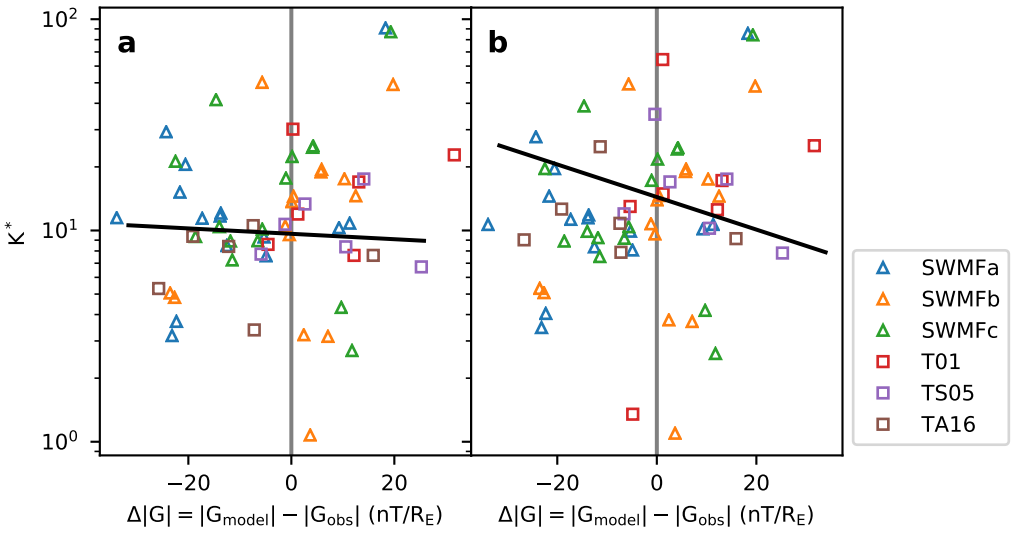

Figure S9: K^* as a function of $\Delta|G|$, the estimation error in the derivative $|G| = |\frac{dB_r}{dz}|$. (a) shows the HL dataset and (b) shows the LL dataset. Both the SWMF simulations and the empirical models are shown. Black lines denotes least-squares fits to the data in log space.

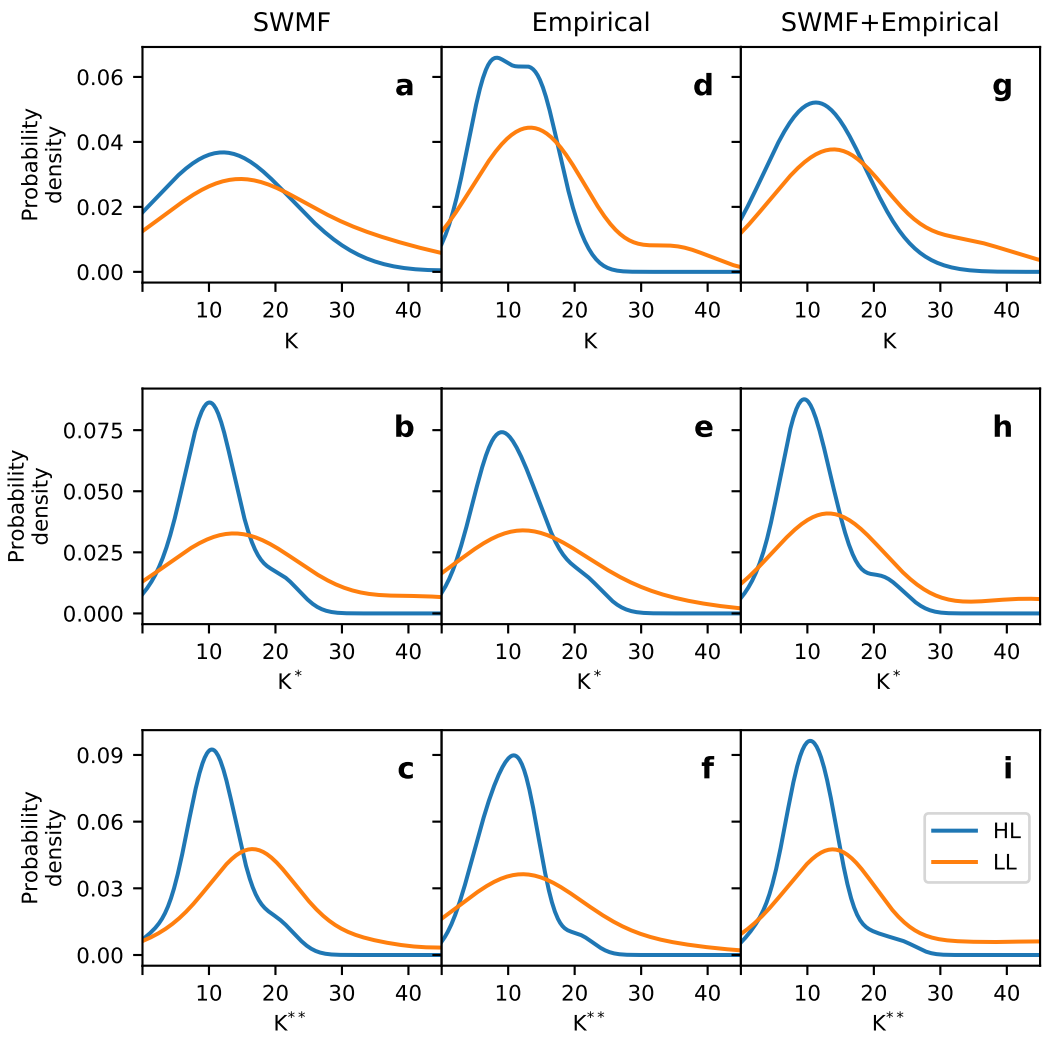

Figure S10: Distributions of K, K^*, and K^{**} from IB observations for which G estimations could be computed. (a) K, (b) K^*, and (c) K^{**} show distributions for all three MHD simulations; (d) K, (e) K^*, and (f) K^{**} show distributions for all empirical models. (g), (h), and (i) show SWMF and empirical models together. The distributions have been separated according to whether the observations came from the high-latitude (HL) or the low-latitude (LL) edge of the IB.

Data Set S1

Data Set S1 contains the IB observations used in the paper. It consists of a ZIP archive containing two files, IBcorr_Conj_HL_GSM.dat and IBcorr_Conj_LL_GSM.dat. These contain data for the HL and LL IB observations, respectively. The files are for-

matted as ASCII text with fixed-width columns. The first row contains a header. The remaining rows contain the following data fields:

- Col. 1-2: Zero-padded 2-digit number identifying the satellite, as follows:
  - 02: METOP-02
  - 15: NOAA-15
  - 16: NOAA-16
  - 17: NOAA-17
  - 18: NOAA-18
  - 19: NOAA-19
- Col. 4-26: Date/time, in the format YYYY-MM-DD/HH:mm:ss.mmm
- Col. 28-30: Day of year
- Col. 32-38: Latitude of IB observation, in AACGM coordinates
- Col. 40-46: Longitude of IB observation, in AACGM coordinates
- Col. 48-53: MLT of IB observation
- Col. 56-63: x (GSM) coordinate of IB observation
- Col. 66-73: y (GSM) coordinate of IB observation
- Col. 76-83: z (GSM) coordinate of IB observation
- Col. 85-: Space-delimited list of spacecraft that were conjugate with the IB, identified as follows:
  - A: THEMIS A
  - D: THEMIS D
  - E: THEMIS E
  - 1: GOES 11
  - 2: GOES 12
  - 3: GOES 13
  - 4: GOES 14
  - 5: GOES 15

Data Set S2

Data Set S2 consists of an HDF5 file containing the IB mapping data presented in the paper. It contains six groups, one for each of the three empirical models and one for each of the three SWMF simulations. Within each group are two sub-groups named "HL" and "LL" (high-latitude and low-latitude) containing results from the high-latitude and low-latitude IB datasets datasets. The "HL" and "LL" groups contain the following data arrays:

- time: Time of IB observation in UTC, formatted as an ISO 8601 string.
- lat: Latitude of the IB observation in altitude adjusted corrected geomagnetic (AACGM) coordinates
- MLT: magnetic local time (MLT) of the IB observation
- dbz: $\overline{\Delta B_z}$, the average error in B_z at the locations of the satellites conjugate with the IB observation
- dg: Estimated error in $G = \frac{dB_r}{dz}$ in the region of probable IB formation
- pos_rmax: Location of the maximum distance from the Earth along the field line traced from the IB location (only provided for SWMF)
- kappa: Adiabaticity parameter $K = \frac{r_c}{r_g}$ at the point of maximum distance along the field line traced from the IB location

Data Set S3

Data Set S3 consists of an HDF5 file containing magnetic field values in GSM coordinates for each of the GOES and THEMIS satellites. It contains four groups, one for each of the SWMF simulations and one for the observational data. Each group contains groups for each satellite, which contain the following data arrays:

- time: Time of the data values in UTC, formatted as an ISO 8601 string
- pos_gsm: Satellite position in GSM coordinates
- B: Magnetic field at the satellite in GSM coordinates

References

Haiducek, J. D., Ganushkina, N. Y., Dubyagin, S., & Welling, D. T. (2019 *accepted*). Relating observed locations of energetic proton isotropic boundaries with mag-

netic field geometry during quiet times. *Journal of Geophysical Research: Space Physics*.